NASA Contractor Report 185300

Solar Rocket Plume/ Mirror Interactions

Sheng-Tao Yu
Sverdrup Technology, Inc.
Lewis Research Center Group
Brook Park, Ohio

Chau-Lyan Chang
High Technology Co.
Hampton, Virginia

Charles L. Merkle
The Pennsylvania State University
University Park, Pennsylvania

January 1991

Prepared for
Lewis Research Center
Under Contract NAS3-25266

National Aeronautics and
Space Administration

SOLAR ROCKET PLUME/MIRROR INTERACTIONS

Sheng-Tao Yu
Sverdrup Technology, Inc.
NASA Lewis Research Center Group
Brook Park, OH 44142

Chau-Lyan Chang
High Technology, Co.
Hampton, VA 23666

Charles L. Merkle
The Pennsylvania State University
Department of Mechanical Engineering
University Park, PA 16802

ABSTRACT

The extent to which the plume from a solar thermal rocket will impinge on the solar collector is studied by flowfield analysis. Such interaction can adversely affect collector performance through fouling, heat loading, or pressure loads that deform the delicate structures. Estimates of these quantities are needed for collector design. The geometrical shape of the collector is such that only the flow from the nozzle boundary layer can reach it, but the thrust levels of interest lead to very viscous nozzle flows with large, thick boundary layers. Reasonable accuracy in solving these flows requires a fully coupled viscous-inviscid procedure inside the nozzle. Results show that the fraction of the plume that hits the collector can be well estimated by continuum theory, but that transitional and rarefied phenomena will have some impact on how it is distributed over the surface. Both the pressure loading and heat flux increase for the smaller thrust sizes, but even for the lowest Reynolds number nozzles increased expansion ratio continues to reduce the interaction. Higher chamber pressure appears to be the most effective way for reducing plume mirror impingement. A factor of two increase in p^0 corresponds to about a factor of five decrease in these impingement parameters.

INTRODUCTION

The concept of solar thermal propulsion is based upon heating a working fluid by concentrated solar energy and expanding it through a standard propulsive nozzle to produce thrust. The complete propulsion system consists of a rocket engine plus a collector to collect and focus the solar energy (Fig. 1). A primary advantage of solar propulsion is that the energy supply need not be accelerated with the vehicle, but remains remote from the spacecraft. The primary challenge of solar thermal propulsion lies in identifying a method for coupling the solar energy into the thermal (kinetic) modes of the working fluid. For this purpose, both direct and indirect absorption concepts have been proposed. Direct absorption requires advanced technology and longer development time. Indirect absorption requires current technology and can be implemented today, although it does suffer some performance penalties in comparison with direct absorption schemes.

In the direct absorption concept, solar radiation is absorbed directly into the flowing gas. Direct absorption of solar energy is difficult because of the low energy densities of the radiation. Even after concentration, solar intensities remain too low to be absorbed readily in most gases of interest. The combination of a trace amount of seedant gas such as alkali metal vapors with a bulk carrier gas such as hydrogen does, however, offer promise of providing acceptable absorption lengths[1]. Analyses of direct absorption in a hydrogen-alkali mixture are presently being conducted[2].

Indirect absorption schemes are those in which the solar energy is incident upon the surface of a heat exchanger. The working fluid is then indirectly heated by passing it over this heated surface. The maximum temperature in such an indirect absorption system is limited by material considerations and in general the full thermodynamic potential of the solar energy cannot be realized. Shoji[3] and Etheridge[4] have shown that through the use of realistic concentrators and high temperature materials, an indirectly heated solar propul-

sion system can provide specific impulses approaching 800 seconds. This performance level is sufficient to provide a 45% increase in payload[4] as compared with conventional chemical propulsion system for a one-way LEO to GEO mission. Construction of an indirectly heated solar thermal demonstration engine based upon these studies is currently underway[5].

The particular aspect of solar propulsion which is addressed in the present paper has to do with the severity of the interaction between the rocket exhaust plume and the solar concentrator. Appropriate geometries can be developed[4] which will ensure that the concentrator will remain outside the direct line of sight of the thrust vector for all orientations with respect to the sun, but the expansion of the exhaust plume away from this direct line of sight and the backflow of small fractions of the plume into the upstream quadrants will lead to plume/mirror impingement. The purpose of the present study is to assess the pressure and heat transfer loads that will be imposed on the mirror by this impingement. The analyses will be limited to technologies based upon indirect absorption.

The size of the collector is dictated by the energy requirements of the engine, which, in turn, are determined by the thrust size and the peak temperature to which the fluid is heated. The peak temperature is set by thermodynamic and material constraints while the thrust size is set by mission requirements. The net effect of these size considerations is a collector that is much larger than the engine. For representative cases, the maximum diameter of the collector is some 5000 times the nozzle throat diameter. Figure 1 also shows that for designs of interest, a plume expansion of about 45° can be tolerated before the plume begins to impinge on the mirror surface.

The peak temperature and the molecular weight of the working fluid determine the specific impulse of the rocket. For the indirect absorption case, the working fluid can be selected on the basis of its molecular weight. Consequently, the properties of pure hydrogen are used here. From second law considerations, the maximum temperature must

lie below the effective temperature of the sun's surface, 5760 K. Peak temperatures in the indirect absorption system are, however, limited by material considerations. The present contamination estimates are based upon a technology that uses rhenium coils for the heat transfer surface[5] corresponding to allowable temperatures of about 2780 K.

In order to estimate the severity of plume-mirror interaction over a range of conditions, a multi-dimensional matrix composed of five different nozzle thrust sizes (5, 50, 250, 500 and 2500 N), three different expansion area ratios (100, 200 and 500 to 1), and two different absorption chamber stagnation pressures was used (3 and 6 atm). Calculations of plume-mirror interactions were made for each element in the matrix for an 80% bell-shaped nozzle[6,7] and for the corner elements in the matrix for a 15° conical nozzle and representative results are included here. A chamber stagnation temperature of 2780 K and a wall temperature of 900 K were used throughout. The nozzle throat radii were determined on the basis of a one-dimensional calculation of the stream thrust for expansion into a vacuum. The working fluid is hydrogen, and for the conditions assumed is taken as having constant specific heats. Sutherland's law was used for viscosity, and a constant Prandtl number was used. Because of the importance of the nozzle wall boundary layer on the degree of impingement, the contamination effects cannot be scaled geometrically but must be recomputed for each thrust level.

PHYSICAL DESCRIPTION OF THE FLOWFIELD

Basic Structure of Exhaust Plumes

It is well known that an inviscid supersonic jet exhausting into a vacuum in constrained by thermodynamics to turn through only a finite angle. At the high supersonic speeds typical of large area ratio nozzles, this maximum turning angle is small, and even with flow angularity present at the nozzle exit, an inviscid jet would remain confined to a narrow angular region in the aft quadrants. This simple description is, however, valid

only for inviscid flows. Any real exhaust flow will also include a boundary layer on its outer periphery. The major fraction of this boundary layer will be supersonic, but a small fraction must be subsonic. The reduced speeds in the supersonic part of the boundary layer allow larger turning angles that can result in impingement on the collector surfaces. The subsonic portions of the boundary layer have no obvious maximum turning limitation but they are accelerated quickly as they exit from the nozzle and will almost certainly be pushed toward the forward hemisphere by the supersonic portions of the boundary layer.

Boundary Layer Transition and Relaminarization

The dominant effect of the boundary layer flow upon the collector impingement problem implies that its development and character must be addressed in detail. The first issue to be discussed is the state of the boundary layer, that is, whether it is laminar or turbulent. The high Mach numbers, wall cooling and strong accelerations that characterize rocket nozzle boundary layers cause them to have considerably different transition characteristics than those observed in typical, incompressible, flat plate boundary layer experiments. The few experimental studies of actual or simulated nozzle boundary layers that have been conducted suggest that transition characteristics can be quite complex[8-10]. In addition to undergoing transition from laminar to turbulent flow, relaminarization from turbulent to laminar flow can also take place. In a typical high Reynolds number nozzle, the initial transition from laminar to turbulent flow occurs in the converging section upstream of the throat. The strong accelerations downstream of the throat can, and frequently do, cause this turbulent boundary layer to relaminarize once again. In high area ratio nozzles the length could be sufficient to allow this relaminarized boundary layer to undergo transition to turbulence a second time. Finally, in small, low Reynolds number nozzles such as those of interest for solar propulsion, the boundary layer could remain laminar all the way from the subsonic region to the exit plane. The experimental data available are not sufficient to provide a complete documentation of transition and relam-

inarization in nozzle boundary layers, but a review of what information is available gives us some guidance as to expected trends.

In experiments conducted in exhaust nozzles, Back and co-workers[8,9] found that the strong acceleration downstream of the throat could suppress turbulence production and cause the boundary layer to revert back to a laminar-like character. Correlations of their data showed that relaminarization occurred for nozzle throat Reynolds numbers below about 2×10^6. Measurements of the heat transfer coefficient[10] showed that it also decreased rapidly when the turbulence intensity decreased.

Experimental studies of the effect of acceleration on an incompressible turbulent boundary layer[10] showed that turbulence generations was inhibited when the parameter, K, defined as,

$$K = \frac{\nu}{u_e^2} \frac{dU_e}{dx}$$

exceeded 3.5×10^{-6}. This parameter is the reciprocal of the Reynolds number based upon the characteristic distance over which the acceleration takes place.

Additional factors such as wall cooling, which has a dramatic effect on boundary layer growth in supersonic flows, will most certainly affect transition and relaminarization, but explicit information on their influences is not available. Perhaps the overriding issue in the present case is the relatively low Reynolds numbers for these small thrust engines. The maximum value of the throat Reynolds number never exceeds 150,000 and drops as low as 5000. Thus, the Reynolds numbers are always as least an order of magnitude below the range where the boundary layer remains turbulent according the Back's criterion. Similarly on the basis of Kay's experimental data, relaminarization occurs immediately after the nozzle throat. Consequently, laminar flows are expected for all cases considered. Despite these indications, attempts were made (as outlined below) to include turbulence effects, but the eddy viscosity never exceeded the laminar value by more than a factor

of fifteen even for the largest nozzles. All implications are that fully turbulent boundary layers are not encountered.

Non-Continuum Effects

In addition to these continuum effects, plume expansion into a vacuum produces transitional and non-continuum effects near the periphery of the plume. The details of this phenomenon have been studied by Bird[12,13,14] using direct simulation Monte Carlo procedures. His analyses show that the non-continuum aspects of an expansion into a vacuum can be characterized by the density gradients along the streamlines. On the basis of Monte Carlo solutions for one-dimensional flows, he defined an empirical breakdown criterion for determining when non-equilibrium effects become significant[12]. He later applied this criterion to Prandtl-Meyer expansions[13] and rocket nozzle flows[14]. The criterion quantifies non-continuum effects as beginning when the non-dimensional parameter, P, defined as,

$$P = \frac{\pi}{4} \frac{\nu q}{p} \left| \frac{d\rho}{ds} \right|$$

exceeds 0.05. Here, q is the magnitude of the flow velocity, ν is the kinematic viscosity, p is the pressure, and $\frac{\partial \rho}{\partial s}$ is the density gradient along a streamline. Regions of the jet where P is less than 0.05 are accurately predicted by continuum theory, while regions where P exceeds 0.05 begin to exhibit non-equilibrium effects.

The location of the $P = 0.05$ curve for nominal solar rocket plume conditions of interest here is given in Fig. 2 which summarizes the various regimes in the exhaust flowfield. This curve lies well inside the rotational flow originating in the boundary layer, and although most of the mass that eventually hits the collector will have undergone some non-equilibrium effects, the amount of mass hitting the mirror can be reasonably well established by continuum theory. Non-equilibrium effects will alter the manner in which the contamination is distributed along the surface, but will have little effect on the fraction of the plume that hits the mirror. Accordingly, the present calculations are based

on continuum approaches.

ESTIMATES OF THE BOUNDARY-LAYER CHARACTER BY VISCOUS/INVISCID PATCHING

Flowfield modeling within the nozzle must take into account the inviscid supersonic character of the main flow, but it must also include the viscous effects near the wall because it is this boundary layer flow that will eventually make its way to the collector. For an initial estimate of the boundary layer characteristics, we use a patched boundary layer/inviscid procedure. These initial estimates show that a completely coupled analysis is necessary, and for our final nozzle flowfield predictions we use the parabolized Navier-Stokes equations.

The patching procedure used for the initial boundary layer estimates was based upon a combination of an inviscid Method of Characteristics (MOC) procedure [15], and a differential boundary layer procedure[16] incorporating a two-layer eddy viscosity model[17]. The inviscid core flow calculations were started from a supersonic starting line taken from an approximate analysis of the transonic flow in the throat region. The pressure distribution obtained from the MOC procedure was then input to the boundary layer analysis to obtain the boundary layer characteristics and displacement thickness.

The characteristics of the boundary layer as determined by the patching procedure are tabulated in Table 1 for five nozzle sizes corresponding to the five thrust levels. To give an indication of the sensitivity to wall temperature, results are shown for four different wall temperatures, 550, 1100, 1650, and 2200 K. Table 1 gives the ratios of the boundary layer thickness, δ^*, at the exit to the nozzle radius at the exit plane, R_e, along with the momentum thickness Reynolds number at the exit, Re_θ. The columns at the far right give the nozzle exit radius in millimeters and indicates whether the calculations are for laminar or turbulent flow. The calculations for the 50 N nozzle were performed for both laminar

and turbulent conditions.

The most striking feature of the Table is the very viscous nature of the flow. The boundary layer thickness, δ, generally reaches halfway to the axis. The displacement thicknesses range for 10 to 50%, and the Re_θ's range from below 100 to only 700 for the largest nozzle. Increased wall cooling reduces both the displacement thickness and the boundary layer thickness, but even at the lowest wall temperature (which is colder than expected wall operating temperatures), the boundary layers remain very thick.

Although these calculations are useful for determining the general characteristics of the nozzle flows, it is clear that the patching between the inviscid and the boundary layer solutions is only satisfactory for the largest nozzle sizes and the coldest wall temperatures and it may be questionable there. A fully coupled procedure that includes the viscous and inviscid effects simultaneously is required.

COMPUTATION OF THE NOZZLE AND PLUME FLOWFIELDS

Parabolized Navier-Stokes Formulation

To solve the boundary layer and inviscid flows in coupled fashion, a parabolized scheme[18] has been selected. The PNS equations are obtained from the compressible Navier-Stokes equations by neglecting streamwise diffusion and making an appropriate simplification in the convective terms. If the complete inviscid terms are retained, the pressure gradient in the streamwise momentum equation will allow information to be propagated upstream when the flow is subsonic and space-marching will not be well-posed. This ill-posedness can be removed by including only a fraction of the pressure gradient in the streamwise momentum equation[19]. Forward marching is allowed if this fraction, ω, satisfies the inequality,

$$\omega \leq \frac{\gamma M^2}{1 + (\gamma - 1)M^2} \tag{1}$$

where γ is the specific heat ration and M is the streamwise Mach number. The remainder, $1-\omega$, of the pressure gradient can be evaluated explicitly using backward differences, but is frequently omitted.

After transforming to generalized body-oriented coordinates and dropping diffusive terms in the streamwise direction, the PNS equations become,

$$\frac{\partial Q}{\partial t} + \frac{\partial E}{\partial \xi} + \frac{\partial F}{\partial \eta} = \frac{\partial V}{\partial \eta} + H - \frac{\partial P}{\partial \xi} \tag{2}$$

The vectors Q, E, and F are,

$$Q = \frac{r}{J}(\rho,\ \rho u,\ \rho v,\ e)^T \tag{3}$$

$$E = \frac{r}{J}\begin{pmatrix} \rho\overline{U} \\ \rho\overline{U}u + \omega p\xi_x \\ \rho\overline{U}v + \omega p\xi_r \\ (e+p)\overline{U} \end{pmatrix} \qquad F = \frac{r}{J}\begin{pmatrix} \rho\overline{V} \\ \rho\overline{V}u + p\eta_x \\ \rho\overline{V}v + p\eta_r \\ (e+p)\overline{V} \end{pmatrix} \tag{4}$$

The viscous flux vector, V, is given by,

$$V = \frac{r}{J}\begin{pmatrix} 0 \\ t_1\frac{\partial u}{\partial \eta} + t_3\frac{\partial u}{\partial \eta} \\ t_2\frac{\partial v}{\partial \eta} + t_3\frac{\partial u}{\partial \eta} \\ t_4\frac{\partial}{\partial \eta}\frac{e}{\rho} + t_3\frac{\partial}{\partial \eta}uv \\ +(t_1-t_4)\frac{\partial}{\partial \eta}\frac{U^2}{2} + (t_2-t_4)\frac{\partial}{\partial \eta}\frac{v^2}{2} \end{pmatrix} \tag{5}$$

where the terms t_1 through t_4 are given by,

$$\begin{aligned} t_1 &= \mu\left(\frac{4}{3}\eta_x^2 + \eta_r^2\right) \\ t_2 &= \mu\left(\eta_x^2 + \frac{4}{3}\eta_r^2\right) \\ t_3 &= \frac{1}{3}\mu\,\eta_x\,\eta_r \\ t_4 &= \frac{k\gamma}{C_p}\left(\eta_x^2 + \eta_r^2\right) \end{aligned} \tag{6}$$

Finally, the source term, H, and the remaining part of the inviscid flux vector, P, are:

$$H = \frac{1}{J}\begin{pmatrix} 0 \\ -\frac{2}{3}\,\eta_x\,\frac{\partial \mu v}{\partial \eta} \\ p - \frac{2}{3}\,\mu\left(\frac{2v}{r} - \eta_x\frac{\partial u}{\partial \eta} - \frac{v\eta_r}{\mu}\frac{\partial \mu}{\partial \eta}\right) \\ -\frac{2}{3}\left(\eta_x\frac{\partial}{\partial \eta}\,\mu uv + \eta_r\frac{\partial}{\partial \eta}\,\mu v^2\right) \end{pmatrix} \tag{7}$$

$$P = \frac{r}{J}(1-\omega)\begin{pmatrix} 0 \\ p\xi_x \\ p\xi_r \\ 0 \end{pmatrix} \tag{8}$$

In these expressions, $\overline{U}$ and $\overline{V}$ are the contravariant velocities, while u and v are the velocities in the axial and radial (x and r) directions, respectively. The coordinate transformation is defined as,

$$\begin{aligned} \xi &= \xi(x,r) \\ \eta &= \eta(x,r) \end{aligned} \tag{9}$$

and J is the Jacobian of the coordinate transformation. For the nozzle problem, the transformation given in Eqn. 9 was defined algebraically. In generalized coordinates, the streamwise Mach number used in the definition of ω in Eqn. 1 becomes,

$$M = \frac{\overline{U}}{c\sqrt{\xi_x^2 + \xi_r^2}} \tag{10}$$

where c is the speed of sound.

Computational Results from the PNS Equations

The numerical solution of Eqn. 2 is generally obtained by dropping the time derivative and marching in x using a non-iterative implicit algorithm[19,20]. The equations can also be solved by marching in time using an appropriate upwind difference for the ξ direction. The present results were computed with such a time-marching scheme that was obtained by

modifying an existing Navier-Stokes code. The time-marching procedure required several iterations at each x step, but allowed the gradient of the flux vector, F, to be differenced in fully conservative form. This improved accuracy means variable x-steps can be used in the time marching procedure without introducing conservation errors, hence, partially offsetting the slowdown due to iteration. In addition, the value of ω was given in Eqn. 1 can be used without a safety factor[18].

Nozzle flowfield solutions for three thrust levels are given in Fig. 3 for the 500:1 nozzle. These results were obtained with the PNS procedure on a 135 x 50 grid. Figure 3a shows the Mach number contours in the 2500 N bell nozzle, while Figs. 3b and 3c show corresponding contours for the 50 and 5 N bell nozzles. As the nozzle size is reduced, the boundary layer thickness increases steadily.

An additional comparison the three of these cases is shown on Fig. 4 which shows the velocity profile at the nozzle exit plane for the 5, 50, and 2500 N bell-shaped nozzles. This figure again shows the increase in viscous effects as the nozzle size is decreased. The differences between the exit profiles in the conical and bell-shaped nozzles for the 2500 N case are also compared here. The different nozzle geometries have a considerable effect on the exit profile. Finally, Fig. 4 shows the exit profile computed with the MOC-boundary layer analysis for the 5 N bell-shaped nozzle for comparison with similar results from the PNS solutions. This profile is for two iterations between the MOC and boundary layer solutions. Further iterations should be included, but this comparison shows the general trend observed, namely that the patched solutions overestimates the thickness of the boundary layer.

Computations of the Exhaust Plume

After the flow inside the nozzle has been computed, the results can be used as the start line for the plume calculation. Following Ref. 15, the plume is divided into two regions, a nearfield region that is treated by the Method of Characteristics, and a farfield region

where a simple expansion flow is assumed. The start line for the plume MOC calculation must include both the inviscid and the boundary layer profile. After the flow leaves the nozzle, the viscous effects in the boundary layer may be ignored, but the rotationality that has been introduced into the flow by the viscosity has a distinct effect on the plume and its effects must be included.

The MOC procedure[15] considers an inviscid, perfect gas with variable specific heats and includes capability for rotational flow and axisymmetric geometries.

The subsonic portion of the boundary layer cannot be handled by an MOC method and accurate solution of this region requires a full Navier-Stokes procedure if a continuum assumption is used. Because a Navier-Stokes procedure would necessitate a major increase in computer resources, the simple ad hoc procedure suggested in Ref. 15 was used. In this procedure, the subsonic part of the boundary layer was accelerated to supersonic speeds and treated as an inviscid rotational flow in the MOC procedure.

Far from the nozzle exit, the flowfield becomes a pure isentropic expansion along each streamline and calculations using MOC become unnecessary. A simple source flow expansion is used to calculate the flow in this farfield region. The switch from MOC to source flow expansion is typically made some 200 nozzle throat radii from the exit plane.

Plume Flowfield Results

A characteristics net as obtained from the MOC solution procedure is shown in Fig. 5 for representative near-field plume conditions. The outer boundaries of the near-field calculation are nominally taken as 50 throat radii from the centerline in the radial direction and 100 throat radii in the axial direction. Characteristic nets like the ones shown in Fig. 5 were obtained for all cases in the test matrix and were used to generate the contour plots discussed below.

Near-field Mach number contour plots for the three cases shown earlier are presented in Fig. 6. These plots show constant Mach number contours for the nearfield plume starting

from the nozzle exit plane and extending to a region where all streamline curvature is gone and the streamlines are completely straight. In general, each constant Mach number contour extends far downstream in regions near the axis, but the contours first return closer to the nozzle at larger angles away from the axis before again extending radially outward in the rotational flow region to form the lobe mentioned earlier. On the outer edge of the plume the Mach number contours all return to the nozzle lip at a common location. These regions of near approach correspond to local regions of high acceleration. The one on the plume edge occurs because of the local expansion. The strong acceleration region at about 30° and the lobe of slower acceleration at about 45° are induced by the total pressure gradient in the boundary layer. It is this lobe with which we are particularly interested in the present analysis because it is this portion of the plume that eventually impinges on the collector.

Comparison of the contour plots for the three thrust levels indicates there is a reduced degree of expansion in the smaller nozzles. The plot for the larger nozzle contains Mach number contours up to $M = 15$ whereas the plot for the smallest nozzle only expands up to $M = 12$ in this same region. The reason is because of the thicker boundary layer in the 5 N nozzle. Also, the low acceleration lobe caused by the boundary layer is observed to increase in size as the thrust level is reduced until at the smallest nozzle size, this lobe nearly dominates the entire flowfield. Similar qualitative comparisons remain true for the other cases in the computational matrix.

These nearfield plume calculations have been extended to farfield locations by the geometrically based method suggested in Ref. 15. A representative pressure contour plot in the farfield is give on Fig. 7. This figure emphasizes the rapid fall-off in pressure in the vicinity of the "shadow" of the nozzle wall.

PLUME IMPINGEMENT CALCULATIONS

The mirror geometry used for the present calculations is shown in non-dimensional form in Fig. 8 for the 3 atm case. Here, the mirror size is normalized by the nozzle throat radius indicating that the physical size of the mirror scales linearly with the geometric size of the nozzle. When the level of pressure in the chamber is changed, however, the nozzle throat size changes accordingly. Thus, although the physical size of the collector for a given thrust size is independent of the chamber pressure, its non-dimensional size is different because r^* changes. For this reason, non-dimensional mirror size for a 6 atm chamber pressure is $\sqrt{2}$ times larger than the one shown in Fig. 8.

The pressure loadings and heat transfer on the front surface of the collector were determined by interpolating farfield solutions like the one on Fig. 7 and are presented in Figs. 9 through 12. The results are presented as plots of the pressure and heat transfer on the front surface of the collector as a function of the arc-length distance along the surface. The arc-length distance is measured from the front, innermost point on the collector.

Figure 9 gives the pressure distribution on the collector for the bell-shaped nozzle for the 3 atm case for pressure area ratios of 100:1 and 500:1. Results are shown for three thrust levels. The results show that the pressure loading on the collector increases as the thrust level is reduced. This is the result of the thicker boundary layer in the lower thrust nozzles. The comparison also shows that higher expansion ratio nozzles also lead to decreased pressure loading on the collector. Even at these low Reynolds numbers, the additional expansion appears to be useful. These pressure loadings, which are in general very low, represent one limitation on the maximum inflation pressures that can be used in the balloon-type mirrors that are presently envisioned[3,4].

Corresponding heat flux results for this 3 atm case are presented in Fig. 10. Similar effects of nozzle Reynolds number and area ratio are seen for the heat flux as were noted for the pressure. The heat flux rates indicated here represent conditions the very thin mirror materials must be able to withstand during solar thruster operation.

Results for a chamber pressure of 6 atm are shown on Figs. 11 and 12. Figure 11 shows the pressure loading while Fig. 12 shows the heat transfer. The effect of Reynolds number is about the same as for the 3 atm case. Comparison between Figs. 9 and 11 shows the pressure loading on the mirror is reduced by a factor of five when the 6 atm chamber pressure is chosen. The reason for this is primarily because of size scaling. Because the thrust levels (and the energy requirements) of the two different chamber pressure nozzles are the same, the collectors are both the same physical size in dimensional coordinates. In non-dimensional coordinates, the collector for the 6 atm nozzle is larger than the one for the 3 atm case. To a first approximation, the pressure fields decay at the same rate in non-dimensional coordinates in the two flowfields, although the pressure level is a factor of two higher for the 6 atm nozzle. The only difference in non-dimensional decay rates is because of the difference in boundary layer characteristics of the two nozzles (which is small). Because the collector is placed in the fringe of the plume where the pressure is falling off very steeply, the high pressure nozzle has considerably smaller pressure loadings. Comparisons of the heat flux rates for the two nozzles (Figs. 11 and 13) show analogous conclusions.

SUMMARY AND CONCLUSIONS

Solar thermal propulsion promises attractive thrust and specific impulse performance for spacecraft operations. One of the technology problems that must be addressed in realizing this performance is the extent to which the exhaust plume interferes with the collector. Proper design can ensure the collector always remains out of the line of sight of the thrust vector, but radial expansion of the plume can still reach the collector surfaces. Only the slower-moving fluid from the nozzle boundary layer can turn far enough to reach the collector. The pressure and heat transfer loads on the surfaces of the solar collectors of a potential solar thermal rocket engine have been estimated on the basis of numerical flowfield

calculations. The results represent important design considerations for the balloon-type collectors that are envisioned. The pressure loads are a necessary input when selecting the inflation pressures to be used inside the balloon. These pressures along with the heat fluxes are needed for selecting the type and thickness of the material to be used for the collector.

Previous design studies[3,4] have shown that the collector surfaces can be placed in locations where the irrotational core flow gases will not hit them directly, but additional plume expansion because of viscous and transitional effects can lead to plume impingement. The present results show that because of the low Raynolds number conditions, the fraction of the plume that hits the collector can be well estimated by continuum methods, although the manner in which the mass is distributed over the surface of the collector may be affected by non-continuum effects. Specifically, only the slower-moving fluid from the nozzle boundary layer can turn far enough to reach the collector. This implies that the boundary layer growth inside the nozzle is of particular interest.

Estimates of the nozzle boundary layer growth show that the small sizes of interest in solar propulsion cause the boundary layer to occupy as muct as 50% of the nozzle radius (75% of the area) at the exit plane. The computation of these viscous flows requires a fully coupled viscous/inviscid procedure. To obtain this coupling we have chosen a parabolized Navier-Stokes formulation. The complete viscous/inviscid profile at the nozzle exit serves as the start line for a rotational Method of Characteristics calculation of the plume. The boundary layer-induced vorticity has a significant effect on the spread rate of the outer edge of the jet and on concentrator impingement. The farfield flow region is handled by an isentropic expansion procedure.

Results of the calculations show that around one to four percent of the jet impinges on the mirrors, but the location and distance are such that the level remains quite benign. Calculations of both the pressure and heat flux show layer interactions for small thrust

sizes where the boundary layers are thicker and the viscous effects are more important.

Despite these viscous conditions, the plume mirror interactions are always decreased by extending the nozzles to large expansion ratios. The increased expansion more than offsets the increased boundary layer growth. Finally, the level of interaction is shown to decrease quite rapidly with an increase in the chamber pressure. Control of chamber pressure thus appears to be the best way to control the interaction phenomena.

ACKNOWLEDGEMENT

This work was sponsored by the Air Force Astronautics Laboratory under Prime Contract No. F04611-84-C-0028.

REFERENCES

1. Mattick, A. T., "Absorption of Solar Radiation by Alkali Vapors", Radiation Energy Conversion in Space, Progress in Astronautics and Aeronautics, Vol. 61, 1978, pp. 159-171.

2. Perry, F. J., "Solar Thermal Propulsion: An Investigation of Solar Radiation Absorption in a Working Fluid", Finala Technical Report AFRPL-TR-84-032, June 1984.

3. Shoji, J. M., "Potential of Advanced Solar Thermal Propulsion", Orbit-Raising and Maneuvering Propulsion: Research Status and Needs, Progress in Astronautics and Aeronautics, Vol. 89, 1984, pp. 30-47.

4. Etheridge, F. G., "Solar Rocket System Concept Analysis", Final Technical Report AFRPL-TR-79-79, Nov. 1979.

5. Selph, C. C. and Maujokas, G. J., "The AFRPL Solar-Thermal Rocket Ativities", paper presented an JANNAF Conference, New Orleans, LA, March 1984.

6. Rao, G. V. R., "Recent Developments in Rocket Nozzle Configurations", APS Journal, Nov. 1961, pp. 1488-1494.

7. Rao, G. V. R., "Approximation of Optimum Thrust Nozzle Contour", APS Journal, Vol. 30, No. 6, June 1960, p. 561.

8. Back, L. H., Massier, P. F., and Cuffel, R. F., "Flow Phenomena and Convective Heat Transfer in a Conical Supersonic Nozzle", J. Spacecraft, Vol. 4, No. 8, 1967, pp. 1040-1047.

9. Back, L. H., Massier, P. F., and Gier, H. L., "Convective Heat Transfer in a Convergent-Divergent Nozzle", Int. J. Heat Mass Transfer, Vol. 7, 1964, pp. 549-568.

10. Back, L. H., Cuffel, R. F., and Massier, P. F., "Laminarization of a Turbulent Boundary Layer in Nozzle Flow-oundary Layer and Heat Transfer Measurements with Wall Cooling", J. of Heat Transfer, August 1970, p. 333.

11. Moretti, P. M, and Kays, W. M., "Heat Transfer to a Turbulent Boundary Layer with Varying Free-Stream Velocity and Varying Surface Temperature-An Experimental Study", Int. J. of Heat Mass Transfer, Vol. 8, 1965, pp. 1187-1202.

11. Moretti, P. M., and Kays, W.M., "Heat Transfer to a Turbulent Boundary Layer with Varying Free-Stream Velocity and Varying Surface Temperature-An Experimental Study" Int. J. of Heat Mass Transfer, Vol. 8, 1965, pp. 1187-1202.

12. Bird, G. A., "Breakdown of Continuum Flow in Freejets and Rocket Plumes", Rarefied Gas Dynamics, Progress in Astronautics and Aeronautics, Vol. 74: Part II, pp. 681-694.

13. Bird, G. A., "Prandtl-Meyer Flow of a Finite Knudsen number Gas", 7th Australian Hydraulics and Fluid Mechanics Conference, Brisban, August 18-22, 1980.

14. Bird, G. A., "Breakdown of Translational and Rotational Equilibrium in Gaseous Expansion", AIAA Journal, Vol. 88, No. 11, p. 1998, 1970.

15. Hoffman,
R. J., Hetrick, M. A. Jr., Nickerson, G. R., and Jarossy, F. J., Plume Contamination Effects Prediction: CONTAM III Computer Program - Vols. I, II and III, Science Applications, Inc., AFRPL-TR-82-033, December 1982.

16. Merkle, C. L., "Stability and Transition in Boundary Layers", Flow Research Report 71, Flow Research, Inc., Went, WA, 1976.

17. Price, J. M. and Harris, J. E., "Computer Program for Solving Compressible Boundary Layer Equations of a Perfect Gas", NASA TM X-2458, Langley Research Center, Hampton, VA, 1972.

18. Anderson, D. A., Tannehill, J. C., and Pletcher, R. H., Computational Fluid Mechanics and Heat Transfer, McGraw-Hill Book Company, 1984.

19. Vigneron, Y. C., Rakich, J. V., and Tannehill, J. C., "Calculation of Supersonic Viscous Flow Over Delta Wings with Sharp Subsonic Leading Edges", AIAA Paper 78-1137, July 1978.

20. Shiff, L. B., and Steger. J. L., "Numerical Simulation of Steady Supersonic Viscous Flow", AIAA Paper 79-0130, January 1979.

TABLE 1

BOUNDARY LAYER CHARACTERISTICS FOR VARIOUS THRUST SIZES

80% Bell-Shaped Nozzle; Area Ration, 100 = 1
$T° = 2780K$, $P° = 3$ atm

Thrust(N)	Para-meter	$T_w(°K)$ 550	1100	1650	2200	R^* (mm)	BL State
5	δ/R_e	.41	.47	.51	.56	1.5	L
	δ^*/R_e	.20	.28	.34	.41		
	$R_e\theta$	46	41	37	33		
50	δ/R_e	.24	.28	.31	.34	4.8	L
	δ^*/R_e	.12	.17	.21	.25		
	$R_e\theta$	81	73	65	58		
50	δ/R_e	.40	.48	.57	.65	4.8	T
	δ^*/R_e	.17	.27	.38	.47		
	$R_e\theta$	130	138	138	133		
250	δ/R_e	.33	.41	.49	.57	15.3	T
	δ^*/R_e	.14	.23	.32	.42		
	$R_e\theta$	231	254	263	259		
500	δ/R_e	.30	.39	.47	.55	34.3	T
	δ^*/R_e	.13	.21	.31	.40		
	$R_e\theta$	299	334	350	349		
2500	δ/R_e	.26	.32	.43	.51	48.4	T
	δ^*/R_e	.11	.19	.28	.37		
	$R_e\theta$	599	650	703	717		

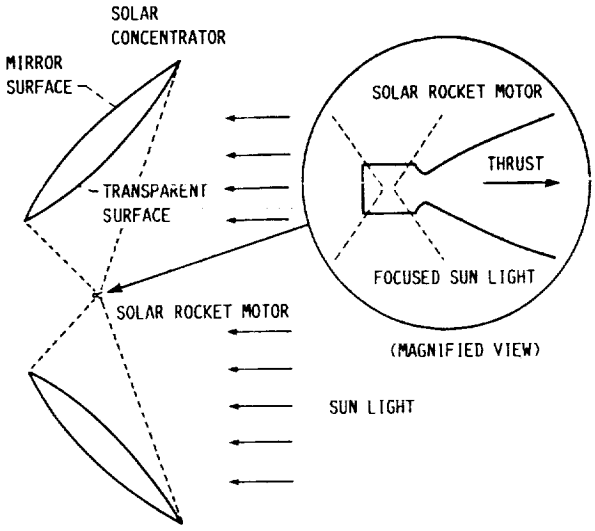

FIGURE 1. - CONFIGURATION OF A SOLAR ROCKET.

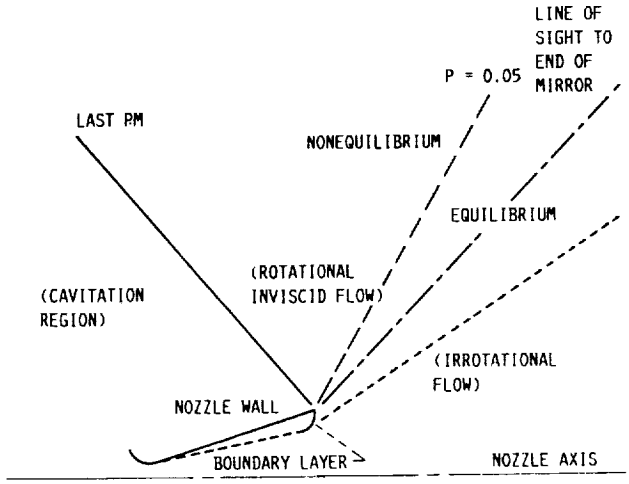

FIGURE 2. - SUMMARY OF DIFFERENT FLOW REGIONS WITH DIFFERENT CHARACTERISTICS.

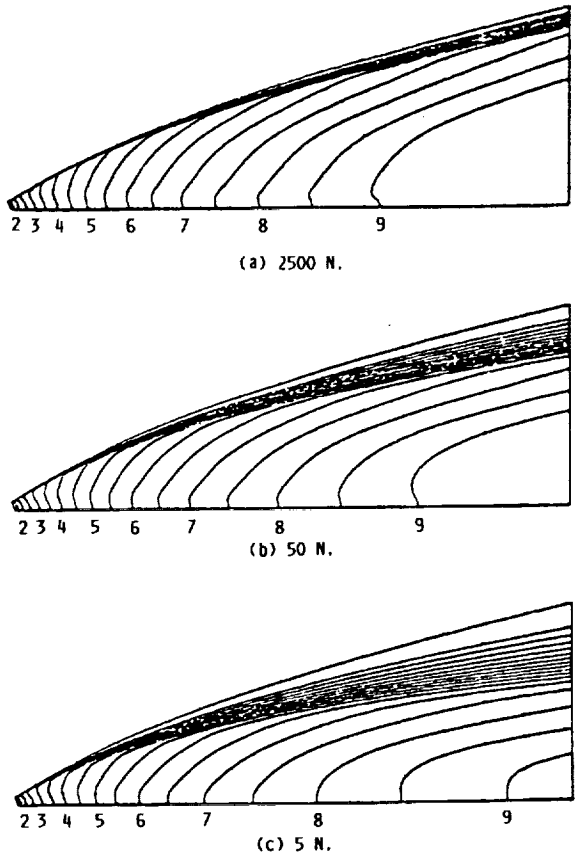

FIGURE 3. - MACH NUMBER CONTOURS FOR VARIOUS THRUST SIZES FOR BELL-SHAPED NOZZLE. AREA RATIO 500:1; P_0 = 6 ATM; T_0 = 2780 K; T_w = 900 K.

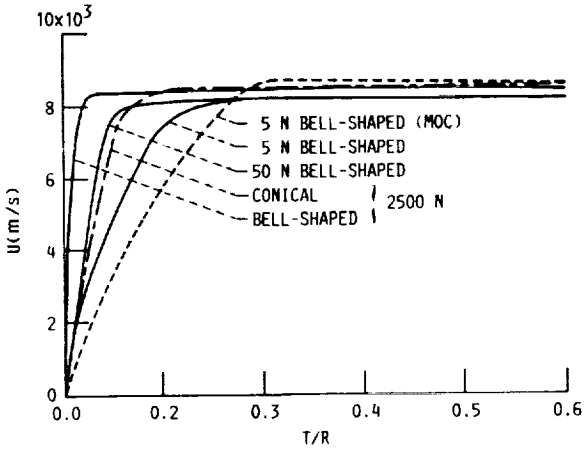

FIGURE 4. - VELOCITY PROFILES AT NOZZLE EXIT PLANE.

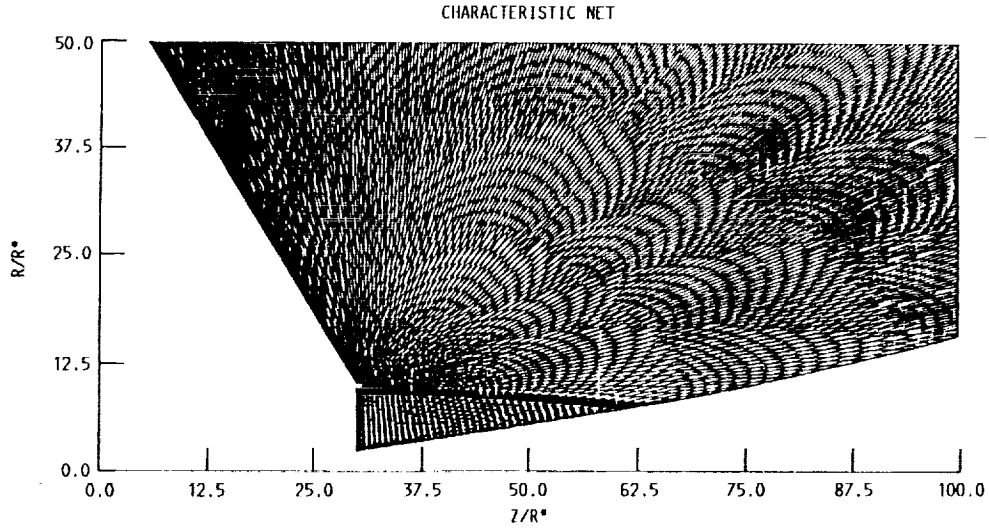

FIGURE 5. - CHARACTERISTIC NET OF THE NEAR-FIELD PLUME FOR THE BELL-SHAPED NOZZLE. AREA RATIO 100:1; P_0 = 3 ATM; T_0 = 2780 K; THRUST LEVEL = 2500 N.

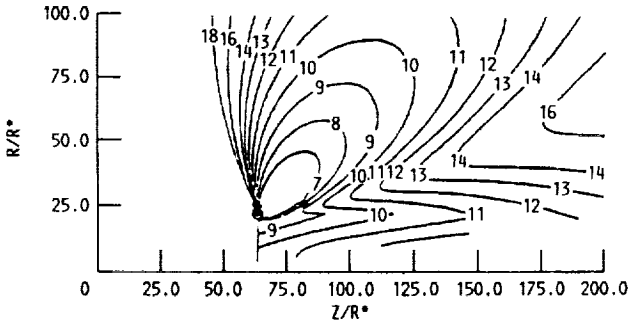

(a) 2500 N.

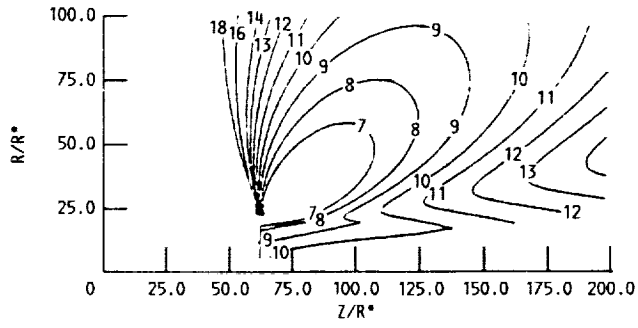

(b) 50 N.

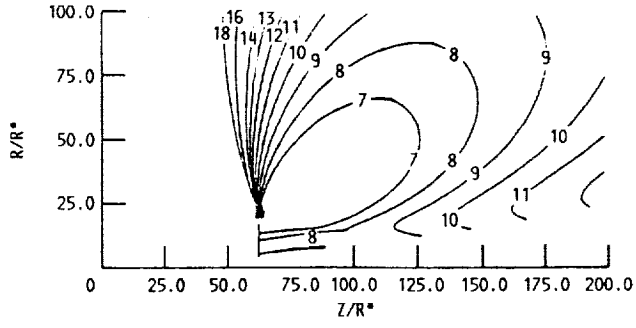

(c) 5 N.

FIGURE 6. - MACH NUMBE CONTOURS OF NEARFIELD PLUME FOR BELL-SHAPED NOZZLE. AREA RATIO 500:1; P_0 = 6 ATM; T_0 = 2780 K; T_w = 900 K.

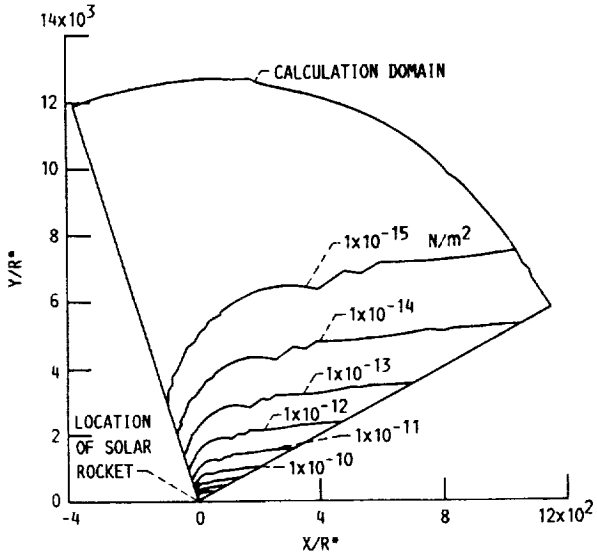

FIGURE 7. - PRESSURE CONTOURS OF FARFIELD PLUME FOR 2500 N BELL-SHAPED NOZZLE. AREA RATIO 100:1; P_0 = 6 ATM; T_0 = 2780 K; T_w = 900 K, R* = 48.4 mm.

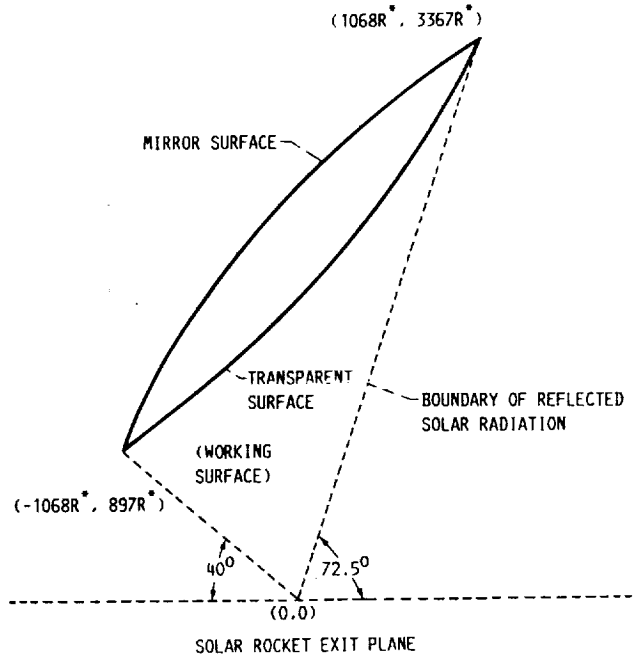

FIGURE 8. CONFIGURATION OF SOLAR CONCENTRATOR (P_0 = 50 PSIA, T_0 = 5000 R).

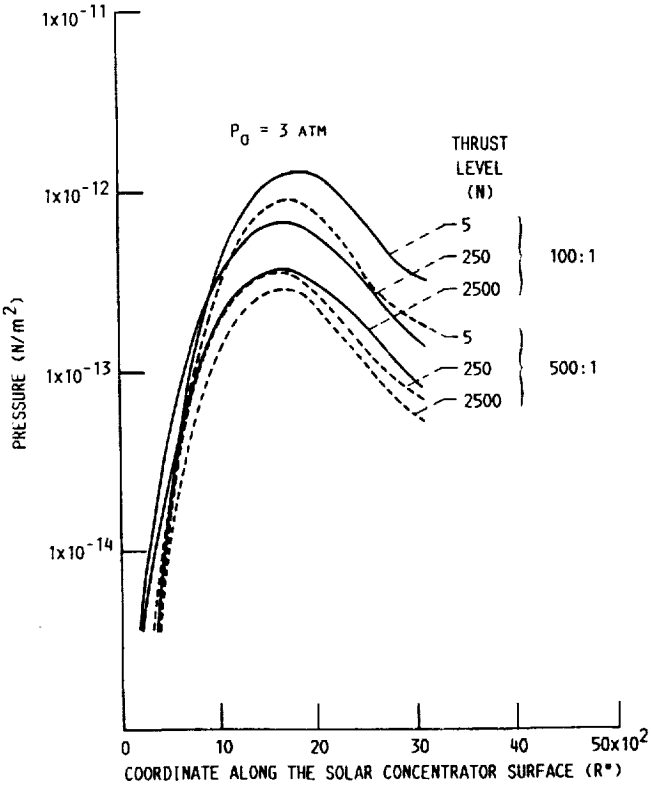

FIGURE 9. - PRESSURE DISTRIBUTION ON THE SOLAR CONCENTRATOR FOR 100:1 AND 500:1 EXPANSION RATIO NOZZLE AT THREE THRUST SIZES FOR THE BELL-SHAPED NOZZLE, P_0 = 3 ATM, T_0 = 2780 K.

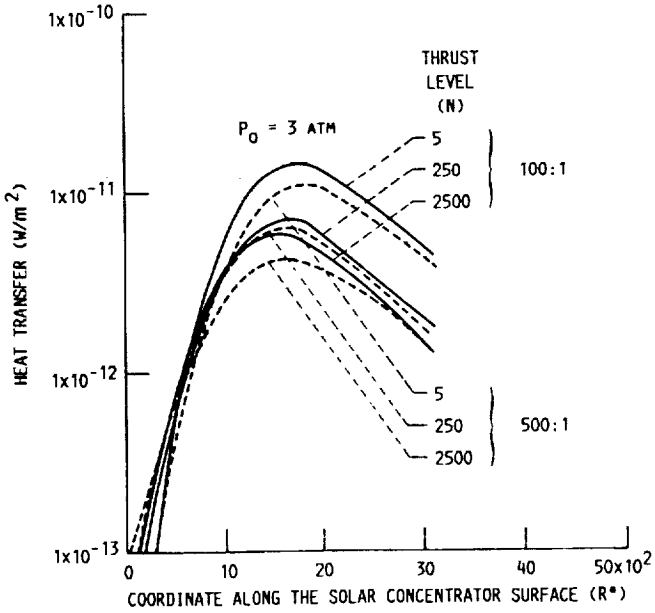

FIGURE 10. - HEAT TRANSFER RATES ON SOLAR CONCENTRATOR SURFACE FOR 100:1 AND 500:1 EXPANSION RATIO BELL-SHAPED NOZZLES AT THRE THRUST SIZES. P_0 = 3 ATM, T_0 = 2780 K.

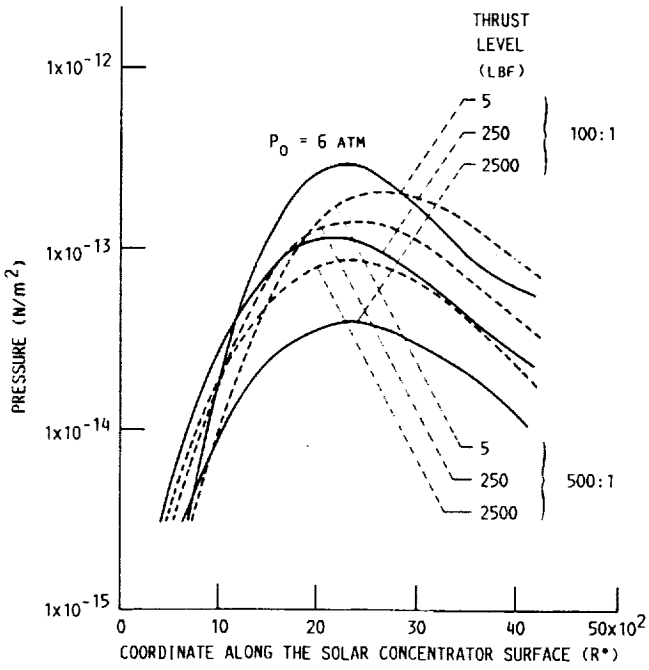

FIGURE 11. - PRESSURE DISTRIBUTION ON SOLAR CONCENTRATOR SURFACE FOR 100:1 AND 500:1 EXPANSION RATIO BELL-SHAPED NOZZLES IN THREE THRUST SIZES. P_0 = 6 ATM.

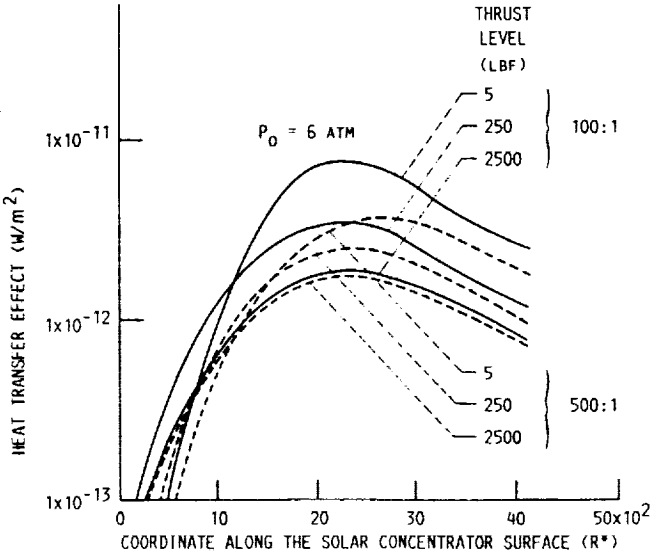

FIGURE 12. - HEAT TRANSFER RATE ON SOLAR CONCENTRATOR SURFACE FOR 100:1 AND 500:1 EXPANSION RATIO BELL-SHAPED NOZZLES AT THREE THRUST SIZES. P_0 = 6 ATM.

NASA
National Aeronautics and Space Administration

Report Documentation Page

1. Report No.	2. Government Accession No.	3. Recipient's Catalog No.
NASA CR-185300		

4. Title and Subtitle	5. Report Date
Solar Rocket Plume/Mirror Interactions	November 1990
	6. Performing Organization Code

7. Author(s)	8. Performing Organization Report No.
Sheng-Tao Yu, Chau-Lyan Chang, and Charles L. Merkle	None (E-5774)
	10. Work Unit No. 505-62-21

9. Performing Organization Name and Address	11. Contract or Grant No.
Sverdrup Technology, Inc. Lewis Research Center Group 2001 Aerospace Parkway Brook Park, Ohio 44142	NAS3-25266
	13. Type of Report and Period Covered Contractor Report Final

12. Sponsoring Agency Name and Address	14. Sponsoring Agency Code
National Aeronautics and Space Administration Lewis Research Center Cleveland, Ohio 44135-3191	

15. Supplementary Notes

Project Manager, Robert M. Stubbs, Internal Fluid Mechanics Division, NASA Lewis Research Center. Sheng-Tao Yu, Sverdrup Technology, Inc. Lewis Research Center Group. Chau-Lyan Chang, High Technology Co., Hampton, Virginia 23666. Charles L. Merkle, The Pennsylvania State University, Dept. of Mechanical Engineering, University Park, Pennsylvania 16802. This work was sponsored by the Air Force Astronautics Laboratory under Prime Contract No. F04611-84-C-0028.

16. Abstract

The extent to which the plume from a solar thermal rocket will impinge on the solar collector is studied by flowfield analysis. Such interaction can adversely affect collector performance through fouling, heat loading, or pressure loads that deform the delicate structures. Estimates of these quantities are needed for collector design. The geometrical shape of the collector is such that only the flow from the nozzle boundary layer can reach it, but the thrust levels of interest lead to very viscous nozzle flows with large, thick boundary layers. Reasonable accuracy in solving flows requires a fully coupled viscous-inviscid procedure inside the nozzle. Results show that the fraction of the plume that hits the collector can be well estimated by continuum theory, but that transitional and rarefied phenomena will have some impact on how it is distributed over the surface. Both the pressure loading and heat flux increase for the smaller thrust sizes, but even for the lowest Reynolds number nozzles increased expansion ratio continues to reduce the interaction. Higher chamber pressure appears to be the most effective way for reducing plume mirror impingement. A factor of two increase in p^o corresponds to about a factor of five decrease in these impingement parameters.

17. Key Words (Suggested by Author(s))	18. Distribution Statement
Solar rocket Plume PNS	Unclassified – Unlimited Subject Category 02

19. Security Classif. (of this report)	20. Security Classif. (of this page)	21. No. of pages	22. Price*
Unclassified	Unclassified	26	A03

NASA FORM 1626 OCT 86

*For sale by the National Technical Information Service, Springfield, Virginia 22161